JGR: Earth Surface

Supporting Information for

Variations in subsidence patterns in the Gulf of Mexico passive margin from Airborne-LiDAR data and Time Series InSAR: Baton Rouge Case Study.

Carolina Hurtado-Pulido[1], Reda Amer[2], Cynthia Ebinger[1], Hayden Holcomb[1]

[1]Department of Earth and Environmental Sciences, Tulane University.

[2]St Louis University, St Louis, Missouri

Contents of this file

Tables S1 to S3

Figures S1 to S10

Text T1 and T3

Introduction

Tables S1 and S2 have additional details regarding the LiDAR and SAR data not included in the main text. Table S3 describes the point samples taken for the time series in figures 4 and 5.

Figures S1 to S10 are mentioned in the main manuscript.

Text T1 to T3 are further explanations of data in the main manuscript.

References cited here can be found in the main manuscript.

Table S1:Characteristics for SAR data for ENVISAT and Sentinel-1 (ESA, 2021a, 2021b).

	ENVISAT-ASAR	**Sentinel-1**
Incidence Angle	23° (scene center)	37-39° (center sub-swath 2)
Polarization	Vertical transmit - Vertical receive (VV)	VV
Pixel dimensions (azimuth x range)	5x25 m	14.1x2.3 m
Swath width (km)	5-1150	250
Average coverage along track (km)	100	22.5-22.7
Average coverage across track (km)	56-100	2.7-3.5
Mean Altitude (km)	800	693
Revisit time (days)	35	12
Images used (First and last lines correspond to the start and end of each file in the column list)	ASA_IMS_1PNESA 20040418_161027_000000182026_00083_11159 20040523_161031_000000182027_00083_11660 20050227_161027_000000182035_00083_15668 20050403_161029_000000182036_00083_16169 20060212_161021_000000182045_00083_20678 20060319_161018_000000182046_00083_21179 20070930_161022_000000182062_00083_29195 20071104_161022_000000182063_00083_29696 20071209_161018_000000182064_00083_30197 20080113_161020_000000182065_00083_30698 20080217_161019_000000182066_00083_31199 20080427_161018_000000182068_00083_32201 20080601_161020_000000182069_00083_32702 20080706_161021_000000182070_00083_33203 20081123_161017_000000182074_00083_35207 20081228_161019_000000182075_00083_35708 20090308_161018_000000182077_00083_36710 20100711_161010_000000182091_00083_43724	S1A_IW_SLC__1SDV_ 20170404T000154_20170404T000221_015987_01A5E6_E689 20170428T000155_20170428T000222_016337_01B092_6BCA 20170522T000156_20170522T000223_016687_01BB42_34B3 20170814T000201_20170814T000228_017912_01E0A9_3885 20170919T000202_20170919T000229_018437_01F0B0_A322 20171013T000203_20171013T000230_018787_01FB66_000F 20171106T000203_20171106T000230_019137_020620_3C80 20180105T000201_20180105T000228_020012_022178_B82A 20180210T000200_20180210T000227_020537_02322D_BEC0 20180306T000159_20180306T000226_020887_023D47_EAF0 20180610T000203_20180610T000230_022287_026979_A6AE 20180704T000205_20180704T000232_022637_0273E0_FF2F 20180902T000208_20180902T000235_023512_028F62_FE69 20181113T000209_20181113T000236_024562_02B230_AD1A 20190112T000207_20190112T000234_025437_02D177_FB1A 20190205T000206_20190205T000233_025787_02DE35_6C0A 20190313T000206_20190313T000233_026312_02F101_7AC1 20190325T000206_20190325T000233_026487_02F77B_E583 20190430T000208_20190430T000235_027012_030AA6_7891

	_0000.N1	20190524T000209_20190524T000236_027362_031615_8339 20190629T000210_20190629T000238_027887_032604_1B81 20190723T000212_20190723T000239_028237_033099_4B20 20190828T000214_20190828T000241_028762_0341E0_CA2A 20190921T000215_20190921T000242_029112_034DFB_8DE7 20191027T000216_20191027T000243_029637_03600E_DBC0 20191120T000215_20191120T000242_029987_036C4D_72A0 20191226T000214_20191226T000241_030512_037E76_0DD0 20200131T000213_20200131T000240_031037_0390C2_751B 20200224T000212_20200224T000239_031387_039CE2_AD2E 20200331T000213_20200331T000240_031912_03AF2A_5844 20200424T000213_20200424T000240_032262_03BB79_34AE 20200530T000215_20200530T000243_032787_03CC40_3FB6 20200729T000219_20200729T000246_033662_03E6C3_D4C6 .SAFE

Table S2: Characteristics for LiDAR point clouds from 1999 and 2018.

	1999	**2018**
Instrument	Leica ALS40	Leica ALS70 HP
Altitude (m)	2,438	1,152
Point spacing (m)	4	0.33
Pulse rate (kHz)	15	450
Vertical Accuracy (cm) -RMSE	15	3.6

Table S3: Description of points for samples of InSAR time series in Figures 4C and 5C.

P#	**Number PS Sentinel**	**Number PS EnviSAT**	**Description**
SJB1	32	16	Points over the building where SJB1 is installed
1	75	31	Points over the Life Storage Baton Rouge, built in ~2004.
2	22	0	Points over homes built in ~2007. Near the fault in the northern block.
3	21	3	Points over homes built in ~2017. Near the fault in the northern block.
4	48	19	Points over the Woman's Hospital built in ~2010. Near the fault in the southern block. This hospital did not exist for Envisat, then these points are from complete area that is the hospital nowadays.
5	74	79	Points at a radius of 160 meters to the injection point with serial number 189576.
6	64	0	Points over the Baton Rouge Wastewater Treatment plant built in ~2009.

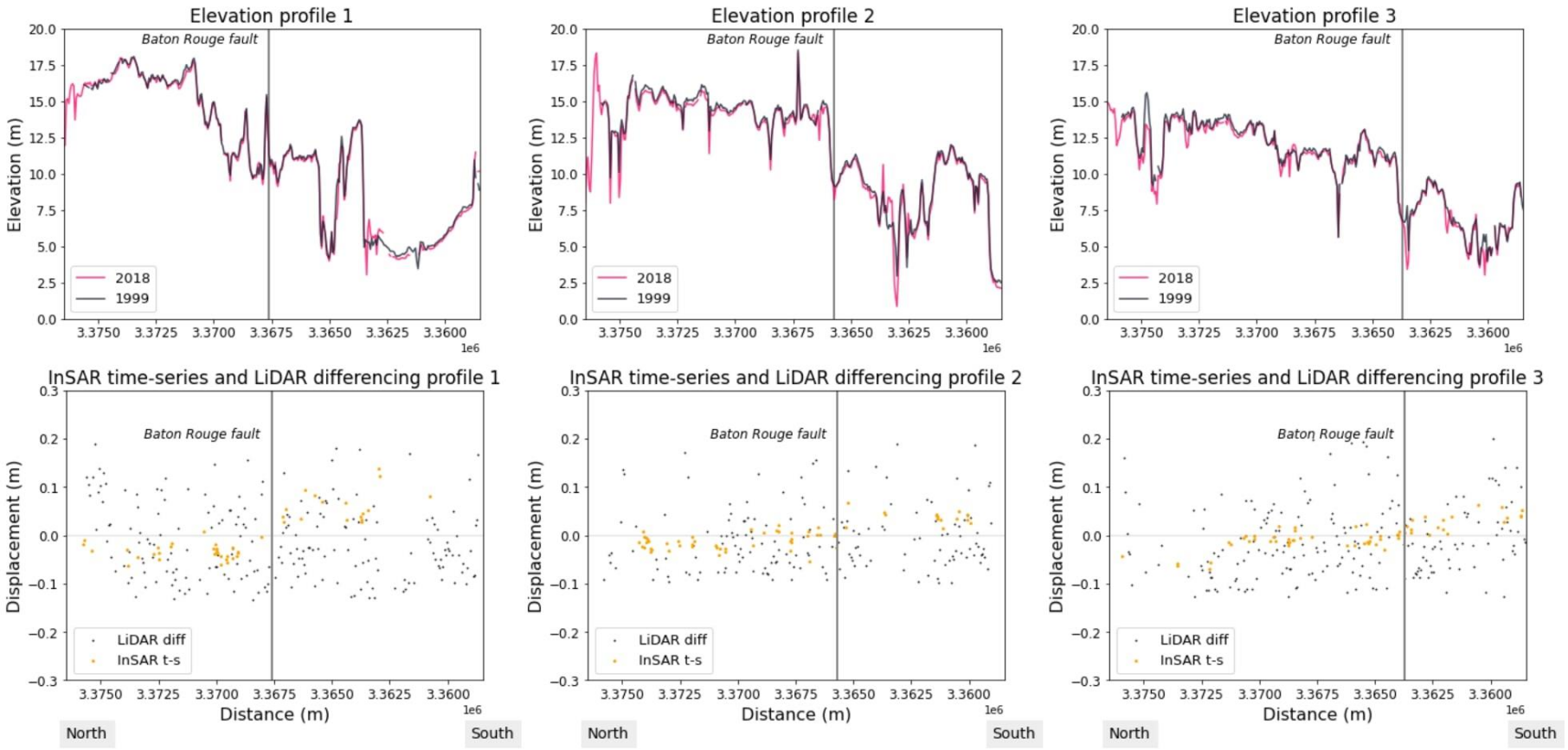

Figure S1: Comparison of elevations using the DEM from 1999 and 2018 in the upper panel and results from our methods along those profiles. For location of the profiles see Figure 2. For the upper profiles, data is averaged every 10 meters from the DEMs, and lower panel is averaged every 20 meters from the LiDAR Vertical difference results (Fig. 8) and the InSAR time-series for Sentinel-1 results (Fig. 4). The time series in the lower panel are not tied to 1LSU reference point.

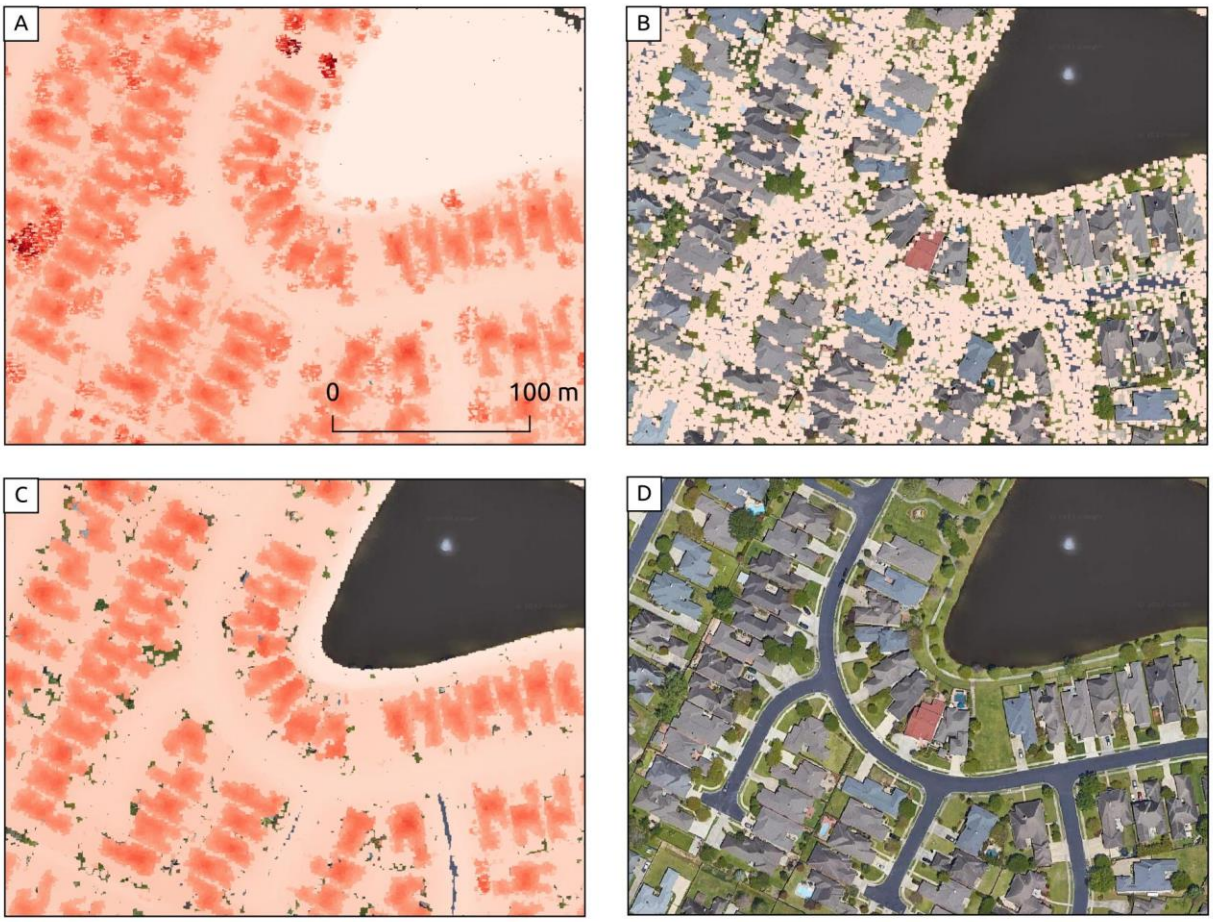

Figure S2: Example of stable surfaces from 2018 LiDAR point cloud. **A)** Original point cloud. **B)** LiDAR points classified by distributor as ground. **C)** Chosen LiDAR points from stable surfaces. **D)** Reference image of the area. Base map imagery from QuickMapServices - QGIS (Map data ©2015 Google).

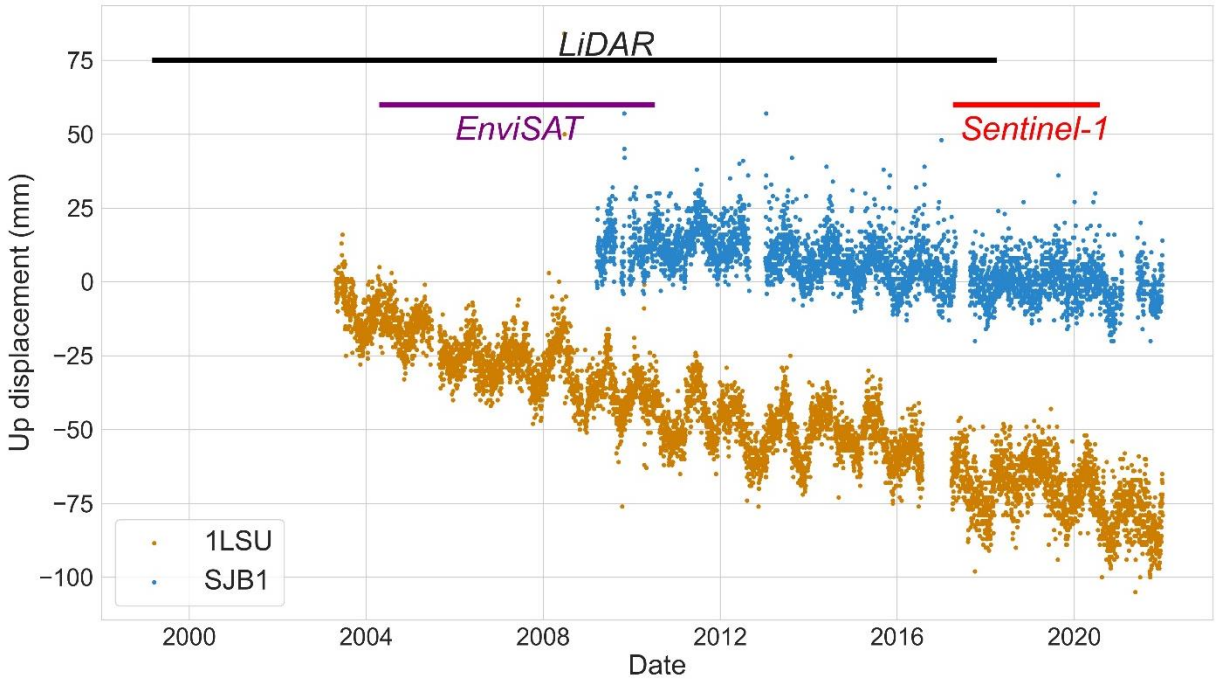

Figure S3: GNSS time series showing the vertical component changes. Horizontal lines labeled as LiDAR, EnviSAT, and Sentinel-1 indicate the time span of these datasets in comparison with the two GNSS time series in the area. GNSS time series are with reference to the fixed North American plate and are from the Nevada Geodetic Survey (Blewitt et al., 2018) and transformed to NAD 83 using the software Horizontal Time-Dependent Positioning from NOAA (Pearson and Snay, 2013).

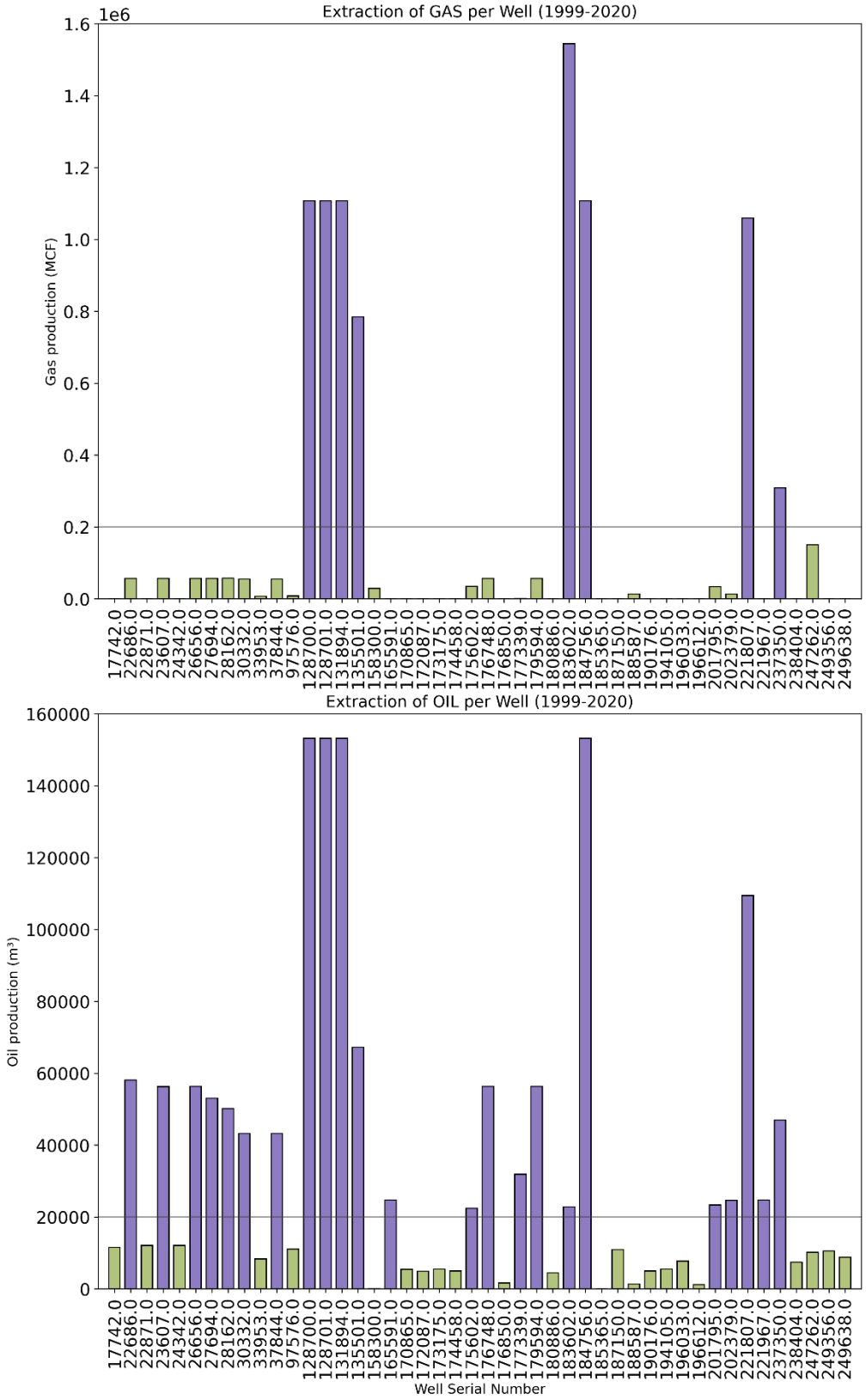

Figure S4: Total gas and oil extracted per well between 1999-2020. Horizontal lines indicate the minimum extraction value to consider a well in our study (200,000 MFC for gas and 20,000 m^3 for oil). Horizontal axis is the well serial numbers. Dark wells extracted more than the threshold value.

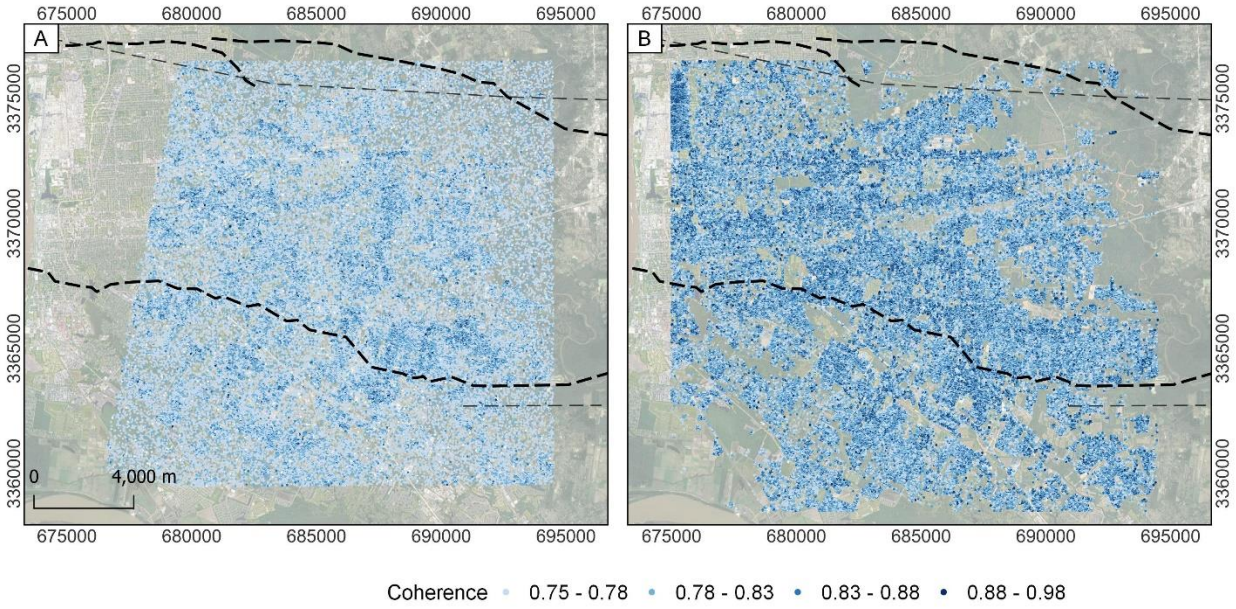

Figure S5: Coherence values for the InSAR time series results. A) EnviSAT coherence for time series between 2004 to 2010, B) Sentinle-1 coherence for time series between 2017 to 2020.

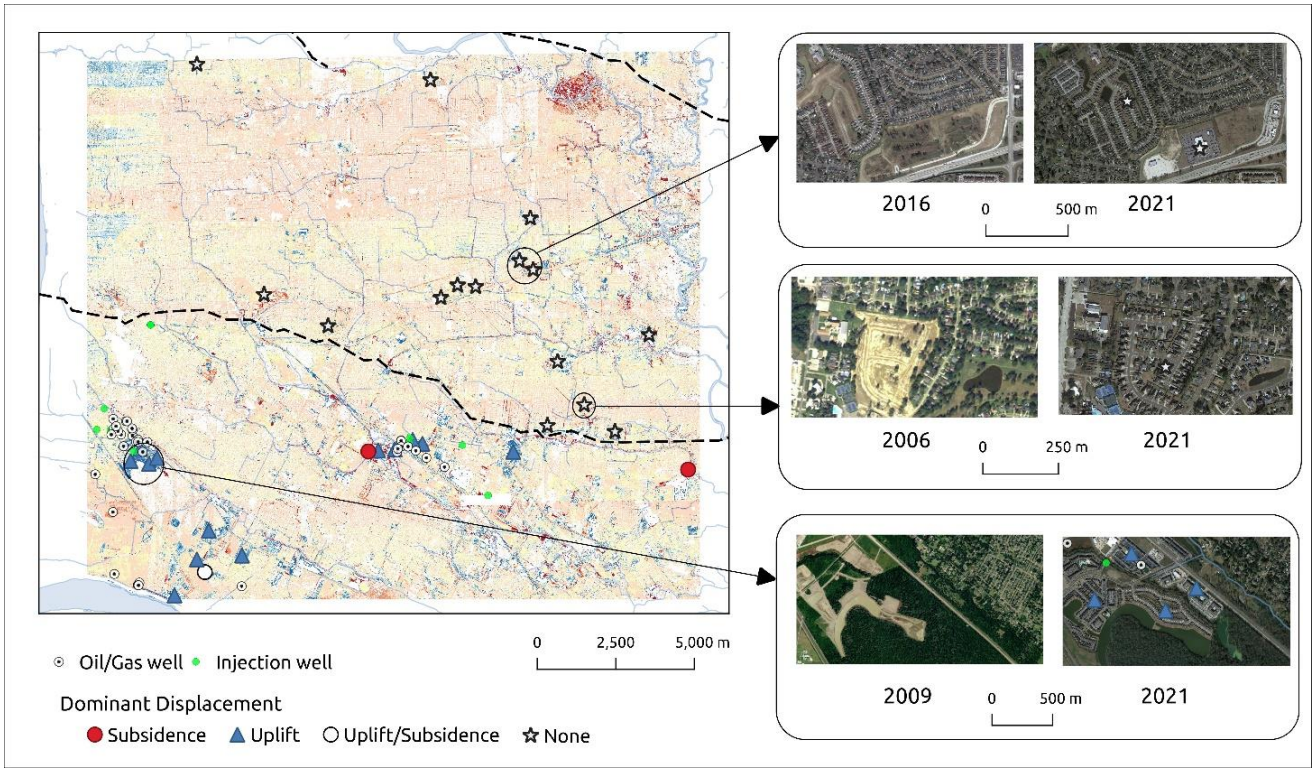

Figure S6: Examples of location of urban constructions built between 1999-2020 and how they look in 2021. Dominant displacement refers to the dominant vertical movement in the area near to the construction. The circle labeled as Uplift/Subsidence encloses the Baton Rouge Wastewater Treatment that encounters uplift to the northwest and subsidence to the southeast. Oil/Gas and injection wells are drawn to compare with building constructions near and far from these wells. Legend for displacement is in Figure 8. Images from 2021 taken from QuickMapServices - QGIS (Map data ©2015 Google). Images from past years are taken from the Historical imagery from Google Earth Pro. Well data from the Louisiana Department of Natural Resources (SONRIS), (n.d.).

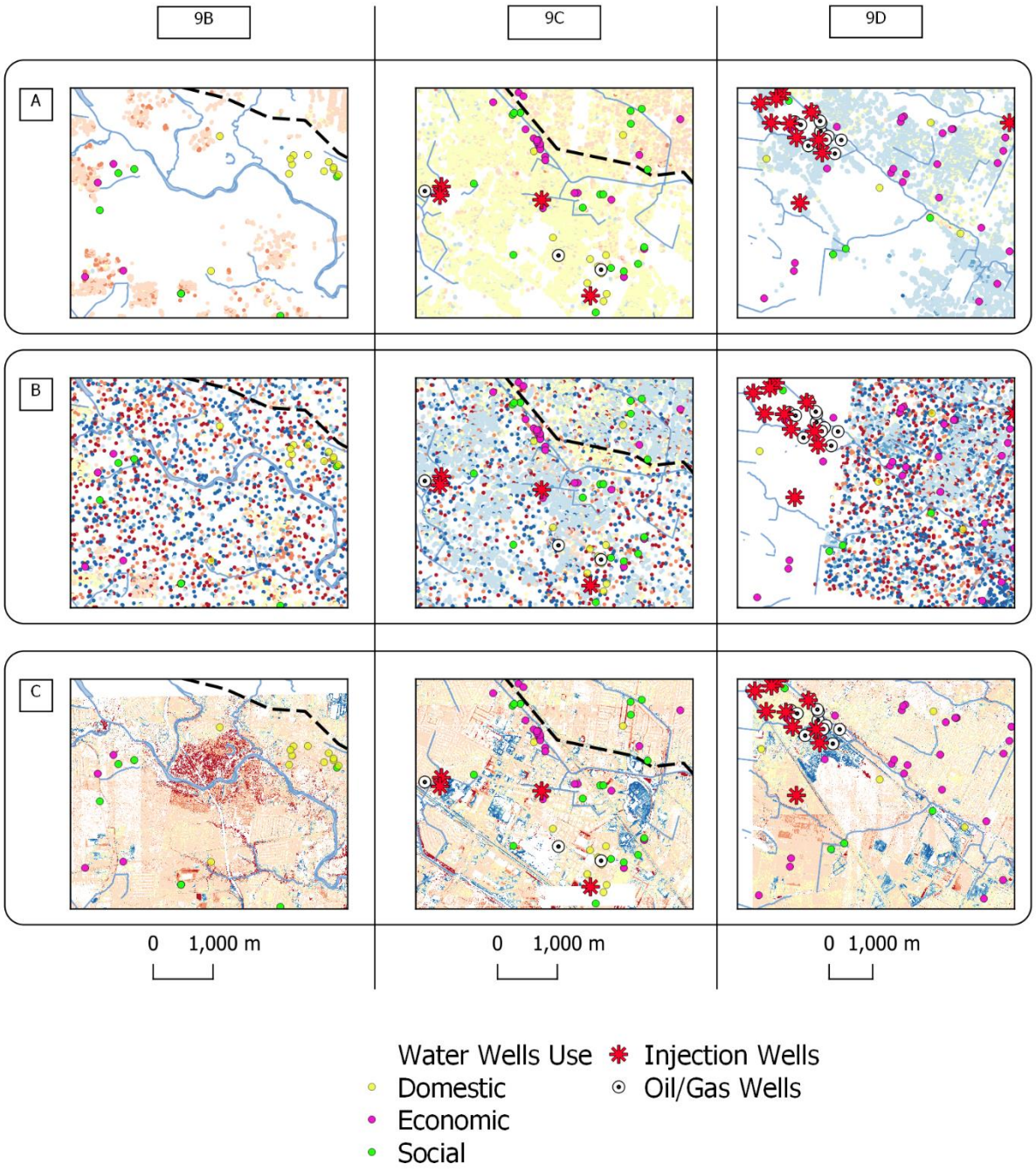

Figure S7: Example of areas experiencing subsidence or uplift determined by different methods compared with injecting and extracting wells. A) Vertical displacement rates calculated with InSAR time series using Sentinel-1 data between 2017-2020. B) Vertical displacement rates calculated with InSAR time series using EnviSAT data between (2004-2010). C) Vertical displacement calculated with LiDAR differencing between 1999-2018. Location of these areas are found in Figure 9. Legend for displacement and rates are in Figures 5 and 9. Well data from the Louisiana Department of Natural Resources (SONRIS), (n.d.)

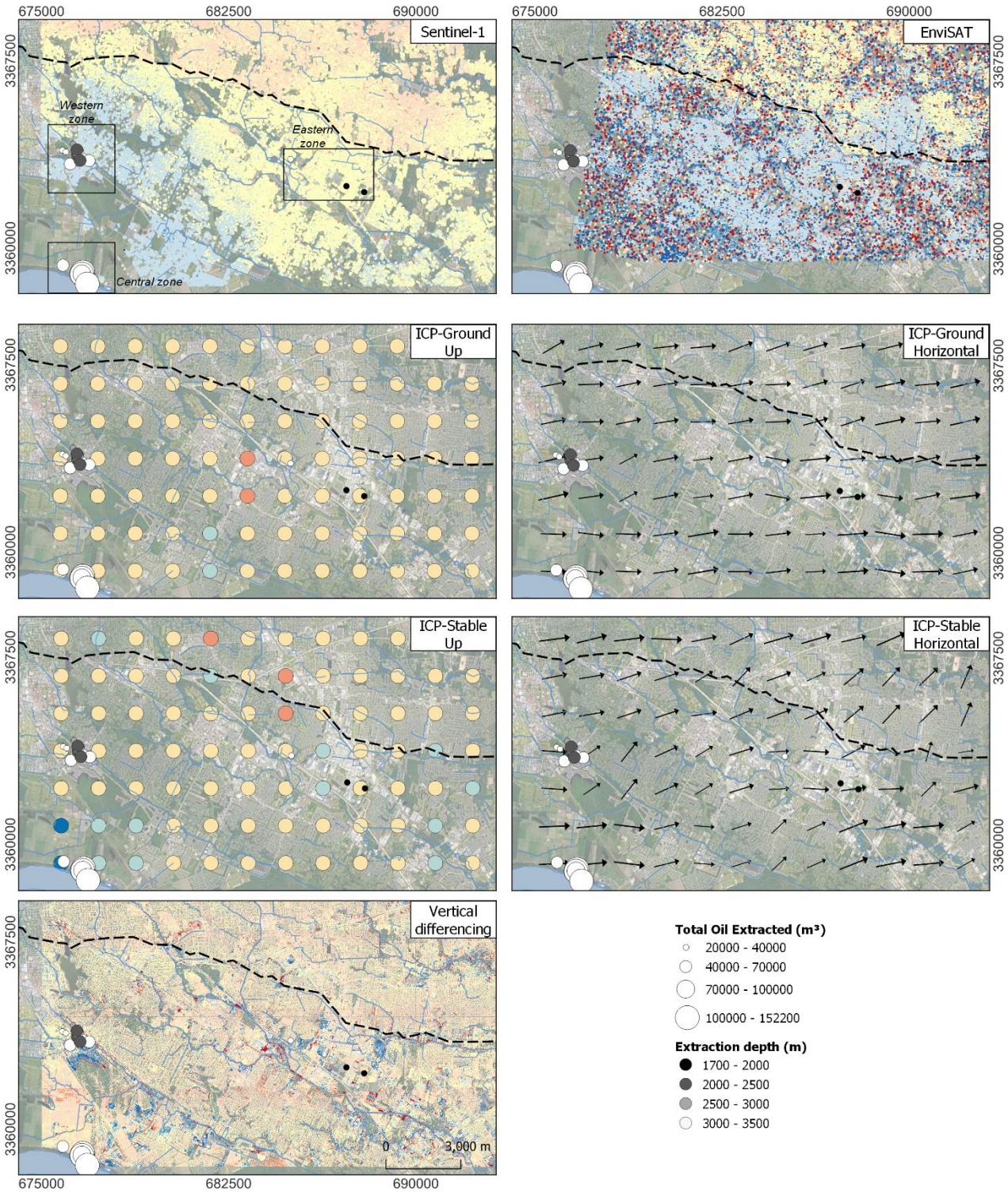

Figure S8: Total oil extracted per well and depth shown in all our results. Method used indicated in the top right corned of each figure.

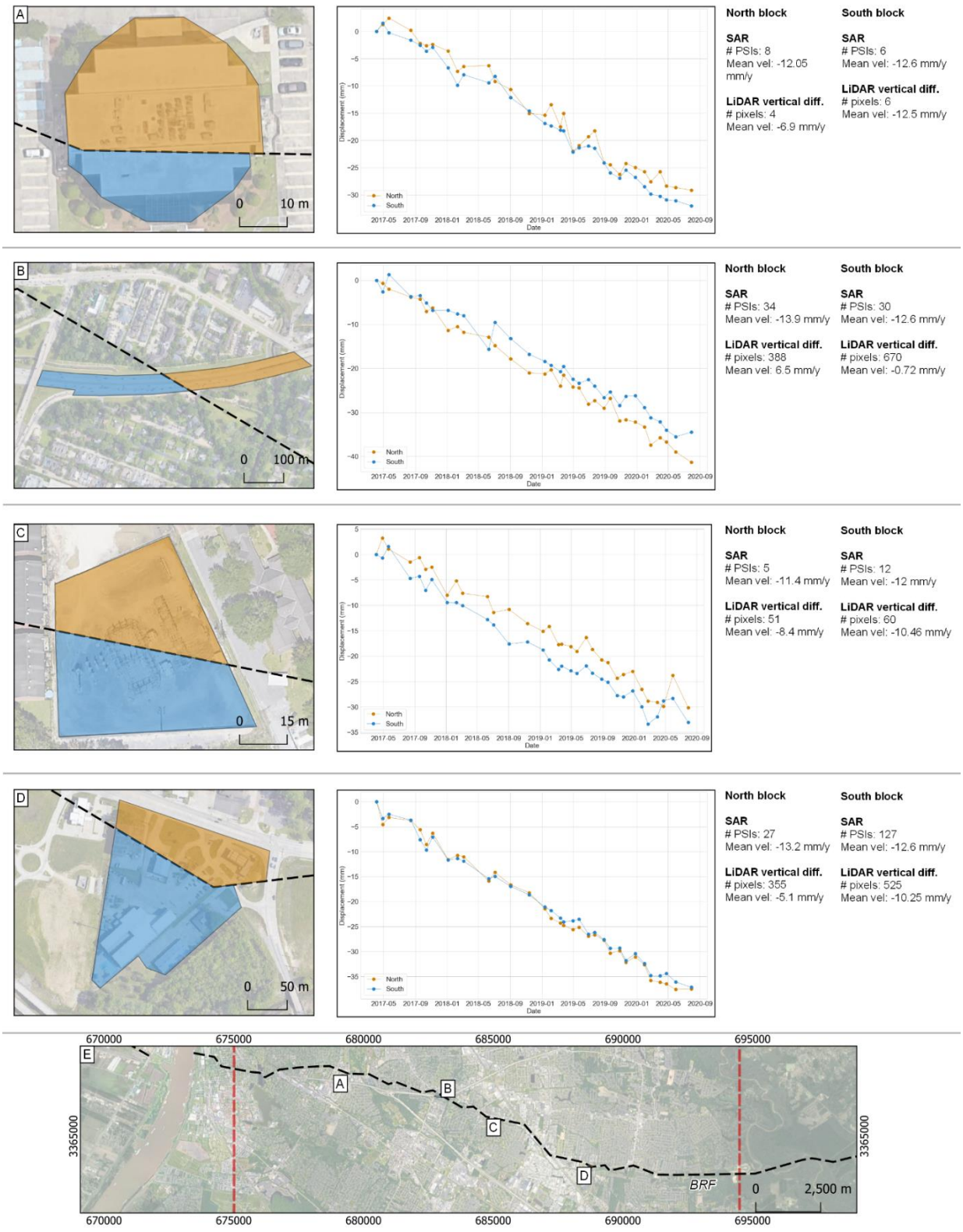

Figure S9: Examples of structures located over the Baton Rouge Fault. The middle column shows the average time series created with the PSIs from Sentinel-1 between 2017-2020 in LOS direction. The right-hand column shows a summary of the results with Sentinel-1 in the LOS direction and LiDAR vertical differencing for the structures. **E)** shows the location of the examples along the Baton Rouge Fault.

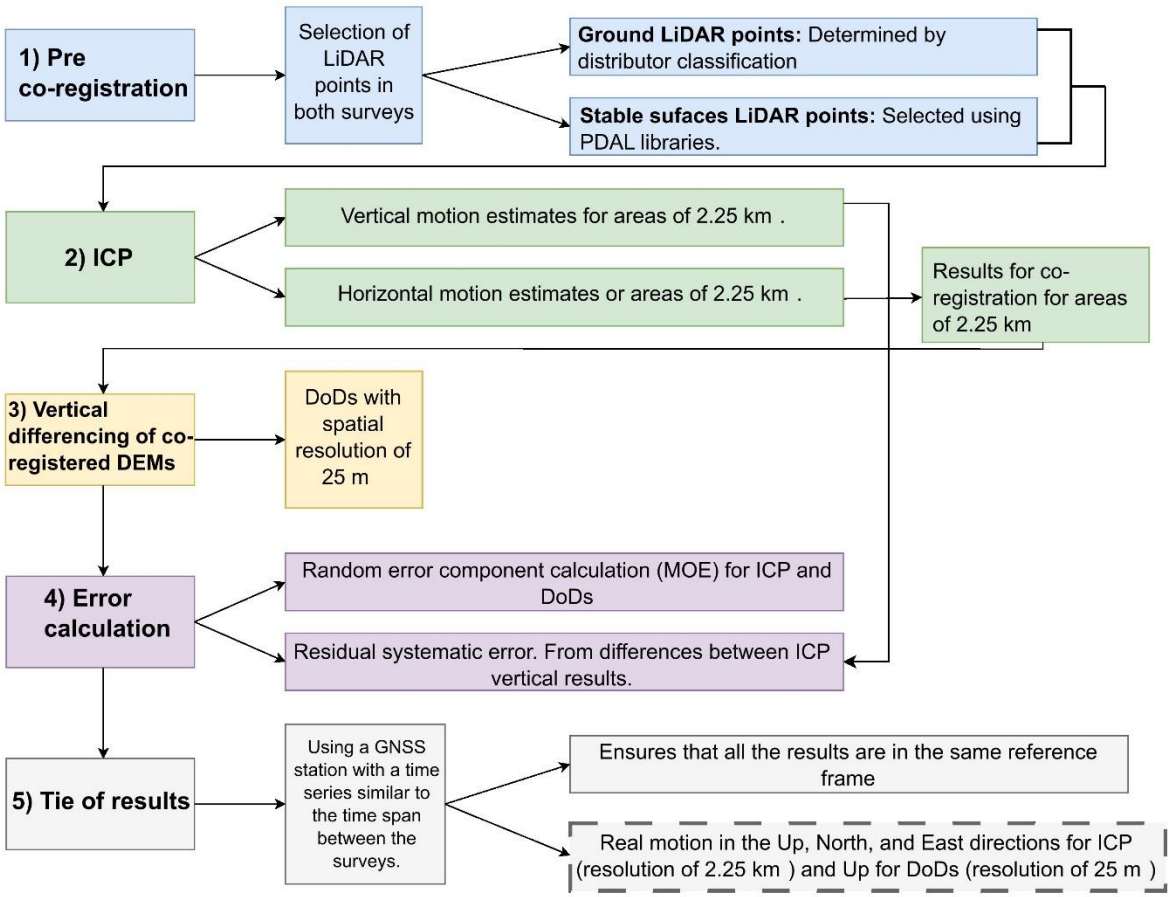

Figure S10: Workflow followed with LiDAR data. Squares with dashed lines indicate results discussed in the text. ICP receives ground LiDAR points and stable surface LiDAR points separately. Details described in the main text.

T1. Brief description of PSI technique with SARscape

The first part of the process is data preparation. It includes co-registration and interferogram generation between the reference image and the other images in the stack, as well interferometric flattening. The topographic phase component is prepared using a DEM to be subtracted from the total interferometric phase. Then, reference points are chosen using the Amplitude Dispersion Index, defined as the temporal average amplitude of a pixel over standard deviation of the amplitude of a pixel**.** Then, the first inversion step is executed. This step calculates displacement velocity and residual height using a linear model for each pixel with respect to the reference points. The model estimates are removed from all the interferograms to recalculate velocity and residual height. Next, the second inversion is applied. At this step the atmospheric phase is estimated to remove spatial and temporal variations from the interferometric phase caused by transmission through the troposphere. SARscape uses water vapor data contained in ENVISAT MERIS, OSCAR (Online Services for Correcting Atmosphere and

Radar), or European Center for Medium-range Weather Forecast (ECMWF) to correct atmospheric disturbances in interferometric pairs. Next, displacements are calculated from the clean interferometric phase for each interferogram. The estimates for displacement and residual heights are recalculated and only pixels with coherence larger than 0.66 are retained. The results are geocoded and exported to raster and vector files (L3Harris, 2014; 2021; Ferretti et al., 2001).

T2. Interpretation S7 - Examples of structures located over the Baton Rouge Fault (BRF)

Here, we present some examples of human-made structures along the BRF. The time series and estimated average for InSAR were calculated using Sentinel-1 data captured between 2017 - 2020 in the LOS direction. LiDAR results correspond to the mean rate motion in the vertical direction calculated using the mean vertical motion that occurred between 1999-2018. The rates calculated with both tools agree in direction but not necessarily in magnitude.

The westernmost structure (Fig. S7-A) shows that the northern block is moving slightly slower than the southern block in the LOS direction, although the results from LiDAR vertical differencing show a large difference between the northern and the southern block of the BRF. The structures in the middle (Fig. S7 – B and C) show more differences between the northern and southern blocks of the fault. Structure B (Highway I-12) shows that the northern block is subsiding faster than the southern block. This persists in the LiDAR results but in this case, the rates are more positive. Structure C shows that the southern block is moving faster than the northern area. It is important to highlight B and C because this area may have more dramatic changes but with opposite creep direction. Finally, the easternmost structure (S7-D) has almost the same motion through time but there are important differences from the LiDAR results.

T3. Empirical tropospheric error estimation with GACOS data

To provide an approximation of the tropospheric delay across the area we present the variation for each interferogram of the time series. We estimate the delay for each interferogram following the instructions included with the GACOS dataset (steps 1 and 2).

1) Tropospheric delay estimated for the EnviSAT time series between 2004-2010 from GACOS data. The average range for the tropospheric delay is 28.75 mm with a standard deviation of 19.26 mm.

Interferogram	Min (mm)	Max (mm)	Range (mm)
200405_200404	-6.0806	2.7735	8.8541
200502_200405	-8.7674	4.7374	13.5048
200504_200502	-4.6723	11.5664	16.2387
200602_200504	-0.6644	0.9008	1.5652
200603_200602	-7.0457	12.4636	19.5093
200709_200603	-37.5965	19.1503	56.7468
200711_200709	-19.4143	39.6906	59.1049
200712_200711	-21.7647	10.5462	32.3109
200801_200712	-1.5267	5.68785	7.21455
200802_200801	-29.2549	17.4207	46.6756
200804_20080217	-19.9467	29.1889	49.1356
200806_200804	-8.35941	16.587	24.94641
200807_200806	-21.7957	12.8036	34.5993
200811_200807	-3.22485	6.35338	9.57823
200812_200811	-18.966	7.65491	26.62091
200903_200812	-18.033	41.5432	59.5762
201007_200903	-16.3195	6.26377	22.58327

2) Tropospheric delay estimated for the Sentinel-1 time series between 2017-2020 from GACOS data. The average range for the tropospheric delay is 35.95 mm with a standard deviation of 18.17 mm.

Interferogram	Min (mm)	Max (mm)	Range (mm)
201704_20170404	-34.0123	10.705	44.7173
201705_201704	-3.46327	19.7599	23.22317
201708_201705	-22.4526	7.8857	30.3383
201709_201708	-5.21444	27.2379	32.45234
201710_201709	-21.4207	9.04634	30.46704
201711_201710	-10.0887	27.6888	37.7775
201801_201711	-5.775	4.51609	10.29109
201802_201801	-9.5724	4.3882	13.9606
201803_201802	-3.0615	21.236	24.2975
201806_201803	-63.766	22.7534	86.5194
201807_201806	-20.4899	49.1851	69.675
201809_201807	-11.0901	10.5169	21.607
201811_201809	-45.635	16.9375	62.5725
201901_201811	-13.6741	39.8819	53.556
201902_201901	-7.68975	7.28437	14.97412
201903_20190313	14.6795	41.2784	26.5989
20190313_20190205	-43.7655	-17.7109	26.0546
201904_201903	-10.0052	15.6866	25.6918
201905_201904	-17.5176	17.7894	35.307
201906_201905	-13.1707	33.0668	46.2375
201907_201906	-33.3431	10.1202	43.4633

201908_201907	-16.5706	23.2875	39.8581
201909_201908	-15.7881	33.9224	49.7105
201910_201909	-4.57821	7.00345	11.58166
201911_201910	-13.0012	6.253	19.2542
201912_201911	-9.38396	13.3874	22.77136
202001_201912	-25.4836	12.6421	38.1257
202002_202001	-8.30461	14.7302	23.03481
202003_202002	-14.4527	42.9988	57.4515
202005_202003	-44.6926	15.8424	60.535
202007_202005	-9.9665	22.3449	32.3114